Nanoscale

Accepted Manuscript

This article can be cited before page numbers have been issued, to do this please use: A. Kajibanga, N. Walden, F. Ngah and M. V. Morrell, *Nanoscale*, 2026, DOI: 10.1039/D6NR00230G.

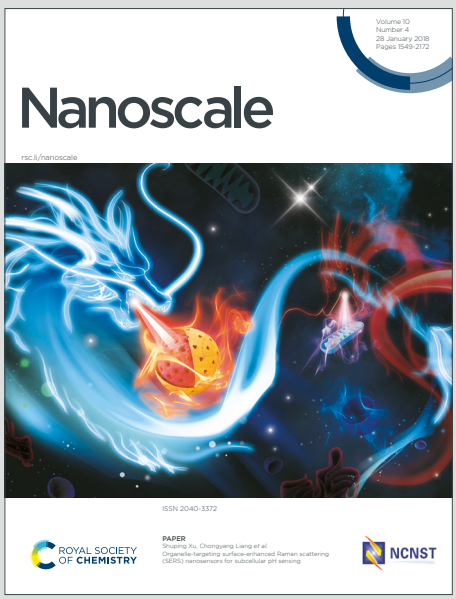

ROYAL SOCIETY OF CHEMISTRY

rsc.li/nanoscale

View Article Online
DOI: 10.1039/D6NR00230G

ARTICLE

Received 00th January 20xx,
Accepted 00th January 20xx

DOI: 10.1039/x0xx00000x

Reassessing the Role of Carbon Shells in Magnetite Nanoparticles: A Comparative Adsorption Study of Ionic Dyes

Anabela Kajibanga, [a] Nathaniel Walden, [a] Franklin Ngah [a] and Maria V Morrell *[a]

Carbon-coated magnetite nanoparticles have been widely explored for water treatment applications; however, the fundamental role, necessity, and true performance advantages of the carbon shell relative to bare magnetite remain insufficiently understood. We present a systematic comparative study of ionic dye adsorption on bare Fe_3O_4 (b-Fe_3O_4) and carbon-coated Fe_3O_4 (c-Fe_3O_4) nanoparticles. Kraft Lignin was the carbon precursor for the carbon shell developed herein. Transmission electron microscopy (TEM) revealed that b-Fe_3O_4 NPs possessed an average diameter of 74 ± 16 nm, while the carbon shell thickness in c-Fe_3O_4 NPs measured 7.2 ± 3.0 nm. BET analysis showed a substantial decrease in specific surface area upon coating application, from 71.30 ± 0.21 m^2/g for b-Fe_3O_4 to 12.01 ± 0.06 m^2/g for c-Fe_3O_4. FTIR spectra confirmed the incorporation of aromatic carbon structures, and XRD patterns indicated identical crystallographic peaks for both samples, demonstrating preservation of the magnetite core. Adsorption experiments with anionic Congo red (CRed) and cationic methylene blue (MBlue) were conducted across a pH range of 2-10. Interestingly, b-Fe_3O_4 NPs exhibited high adsorption of cationic CRed (more than 90%) throughout the entire tested pH range, while displaying negligible adsorption of anionic MBlue. In contrast, c-Fe_3O_4 showed minimal interaction with CRed except at pH 2, but achieved strong MBlue removal, reaching 85% at pH 10. Kinetic analyses revealed rapid CRed uptake by b-Fe_3O_4, reaching equilibrium within ~10 minutes at pH 4, whereas c-Fe_3O_4 required more than 24 hours to reach equilibrium for both dyes. Isotherm studies further confirmed distinct adsorption behaviors associated with each material system. These findings highlight that bare magnetite offers superior performance for anionic CRed, whereas carbon coating selectively improves uptake of cationic MBlue, highlighting that the benefits of carbon shells are system-dependent rather than universal.

Introduction

Over the past decades, substantial progress has been made in the development of surface-functionalized magnetite nanoparticles (NPs), particularly those encapsulated with carbon-based shells. These nanocomposites typically consist of an iron oxide (Fe_3O_4) core encapsulated with a carbon shell, derived from a variety of precursors, including glucose, sucrose, kraft lignin, oleic acid, and polymer-based resins among others.[1-9] Carbon-coated magnetite (c-Fe_3O_4) NPs integrate the advantageous properties of both components: they retain the inherent magnetic properties of the magnetite core, while displaying enhanced chemical stability, improved biocompatibility, and resistance to oxidation compared to bare magnetite (b-Fe_3O_4) NPs.[2-4,10] In addition, the presence of a carbon shell mitigates the strong tendency of b-Fe_3O_4 NPs to agglomerate, thereby improving their colloidal stability and effective surface area.[11] Owing to these properties, c-Fe_3O_4 NPs have been extensively explored as the adsorbents for a wide range of environmental contaminants, including per- and polyfluoroalkyl substances, phenolic compounds, and synthetic dyes.[12-15]

While being widely favoured among researchers, the fabrication of c-Fe_3O_4 NPs requires additional synthesis steps, increased processing time, and higher material complexity. Consequently, a fundamental understanding of the role, the necessity of the carbon shell, and the extent to which it enhances adsorption performance relative to b-Fe_3O_4 NPs is critically important. Most existing studies place emphasis on the design and optimization of core-shell structures and provide the in-depth analyses of their adsorption capabilities, while the b-Fe_3O_4 NPs remain overlooked or implicitly assumed ineffective as standalone adsorbents. Yet, emerging evidence suggests that b-Fe_3O_4 NPs can play a significant role in the adsorption processes and can even enhance the performance of well-established carbon-based adsorbents.[16-20] For instance, Xu et al. demonstrated that the incorporation of b-Fe_3O_4 NPs into the granular activated carbon significantly enhanced its adsorption capacity toward perfluorooctanoic acid, highlighting the active role of b-Fe_3O_4 NPs in the overall adsorption mechanism.[16] Noteworthy, the underlying mechanism governing adsorption processes by b-Fe_3O_4 NPs has yet to be thoroughly elucidated.

Comparative adsorption studies of dyes on b- and c-Fe_3O_4 magnetite NPs have been reported by several groups. However, most of these investigations considered only a single class of dye – either anionic or cationic.[21-26] In studies where both types of dye were considered, the adsorption experiments were conducted only with c-Fe_3O_4 NPs.[15,27] To the best of our

[a] Department of Chemical Engineering, University of North Dakota, Grand Forks 58202 USA. Email: mariia.goriacheva@und.edu; Tel: +1(701)777-4562

View Article Online
DOI: 10.1039/D6NR00230G

knowledge, only one comprehensive comparative study has investigated both types of magnetite NPs in combination with both cationic and anionic dyes.[28] Nevertheless, the experiments in that work were conducted at a single pH value, thereby neglecting the influence of NPs surface charge and dye ionization. Consequently, the authors concluded that c-Fe_3O_4 do not adsorb cationic dyes. In contrast, our results indicate that the adsorption process of cationic dye on c-Fe_3O_4 is possible under specific conditions, such as at pH 2. Therefore, a systematic comprehensive study examining the adsorption kinetics and equilibrium of both b- and c-Fe_3O_4 NPs encompassing cationic and anionic dyes across a broad pH range has yet to be reported.

Addressing this knowledge gap, the present work systematically evaluates and compares the adsorption behaviour of b-Fe_3O_4 and c-Fe_3O_4 NPs across a pH range of 2-10 in the presence of two ionic dyes: anionic Congo red (CRed) and cationic Methylene blue (MBlue). The opposite charges of the dyes allow us to explore the effect of the NPs overall surface charge on the adsorption process. Furthermore, the ionic nature of dyes, together with the aromatic structures, allow simultaneous evaluation of multiple adsorption mechanisms, including electrostatic attractions and π-π interactions. Kraft lignin was selected as the carbon precursor for the shell owing to its abundant functional groups, aromatic structures, and established relevance in wastewater treatment applications.[29-31] The findings of this study also contribute to a deeper understanding of the adsorption mechanism of b-Fe_3O_4 NPs. By critically assessing the strengths and limitations associated with the carbon shell incorporation, especially with respect to dye charge and structure, this work identifies the conditions under which the application of carbon shell is advantageous and offers new insights into the rational design of magnetite-based nanomaterials for environmental remediation.

Materials and Methods

Chemicals and Materials

The following materials were used without further purification: iron (III) hexahydrate trichloride ($FeCl_3{\cdot}6H_2O$, Thermosphere Scientific, 97.0–102.0%), polyethylene glycol 4,000 or PEG ($C_{2n}H_{4n}O_n$, Thermo Fisher Scientific, 99%), sodium acetate or NaAc (CH_3COONa, Thermo Fisher Scientific,99%), ethylene glycol ($C_2H_6O_2$, Thermo Fisher Scientific, 99%), kraft lignin (Sigma Aldrich), Congo red ($C_{32}H_{22}N_6O_6S_2 \cdot 2Na$, Sigma Aldrich, High Purity), and methylene blue ($C_{16}H_{18}CN_3S \cdot xH_2O$, Sigma Aldrich, ≥82%).

Synthesis of b-Fe_3O_4 NPs

b-Fe_3O_4 NPs were synthesized using solvothermal method, previously reported by Deng et al.[32] In short, 1.35 g of $FeCl_3{\cdot}6H_2O$ was added to 40 mL of ethylene glycol and stirred until an orange clear solution was formed. Next, 3.6 g of NaAc and 1 g of PEG were introduced, accompanied by vigorous stirring. The entire mixture was then transferred to a 50 mL Teflon-lined autoclave reactor and baked at 200°C for 8 hours. The resulting black solution was washed twice with DI water-ethanol solution (1:1 ratio) and centrifuged at 4000 rpm for 20 minutes. Probe sonication at 30% amplitude was applied for 3 minutes to disperse the nanoparticles in-between centrifugations. The final wash was done with DI water only and separated via magnetic decantation. The product was freeze-dried and grinded gently to form a thin black powder.

Synthesis of c-Fe_3O_4 NPs

The surface of b-Fe_3O_4 NPs was modified by adding a kraft lignin shell using hydrothermal method. In short, 0.250 g of kraft lignin and 0.100 g of previously synthesized b-Fe_3O_4 NPs were added to 10 ml of DI water. The solution was then transferred to a 50 mL Teflon-lined autoclave reactor and baked at 180°C for 12 hours. The resulting solution was purified with DI water repeatedly to remove unreacted carbon using magnetic decantation. Purification was repeated 8 times. Finally, the product was freeze-dried and lightly milled to form a thin brown powder.

Characterization of c-Fe_3O_4 and b-Fe_3O_4 NPs

Transmission Electron Microscope (TEM) images and elemental mapping were obtained using Talos F200X transmission electron microscope. X-ray Diffraction (XRD) spectra of powders (vacuum-dried at 64˚C) were collected using a Rigaku SmartLab X-ray diffractometer. Fourier Transform Infrared Spectroscopy (FTIR) spectra were measured on the Bruker Invenio-X FTIR spectrometer using a Ge ATR accessory and a room temperature detector. Adsorption spectra were collected using a Genesys 50 UV-visible spectrophotometer. Zeta potential was measured using Malvern zeta sizer. Multi-point BET specific surface area was determined using the Micromeritics Tristar II 3020 gas physisorption analyser (static volumetric method, with nitrogen gas). The samples were degassed under vacuum at 40°C for 1 hour prior to analysis. Magnetic behaviour of b-Fe_3O_4 and c-Fe_3O_4 was analysed by a Quantum Design MPMS-3 SQUID magnetometer.

Adsorption Experiments

For pH-dependence adsorption experiments, 20mL of MBlue or CRed (20 $mg{\cdot}L^{-1}$) solution was prepared using 0.01M NaCl solution adjusted to the desired pH values (2-10). Subsequently, 20 mg of the NPs were added to each solution, followed by probe sonication at 60% amplitude for 1 minute to ensure uniform dispersion. The samples were then placed on the orbit shaker at 150rpm for 24 hours to reach equilibrium.

Kinetics adsorption experiments were conducted at the pH values corresponding to the highest removal efficiency of MBlue and CRed. b-Fe_3O_4 (20 mg) or c-Fe_3O_4 (50 mg) NPs were added to 100 mL of corresponding dye solutions (20 $mg{\cdot}L^{-1}$). At the predetermined time intervals, 1.5 mL samples were withdrawn for the UV-vis absorption measurements.

In adsorption isotherm studies, 20 mg of b-Fe_3O_4 or c-Fe_3O_4 NPs were added to 20 mL of MBlue or CRed solutions, with initial concentrations ranging from 10 to 250 mg·L-1. The solutions were adjusted to the corresponding optimal pH values

View Article Online
DOI: 10.1039/D6NR00230G

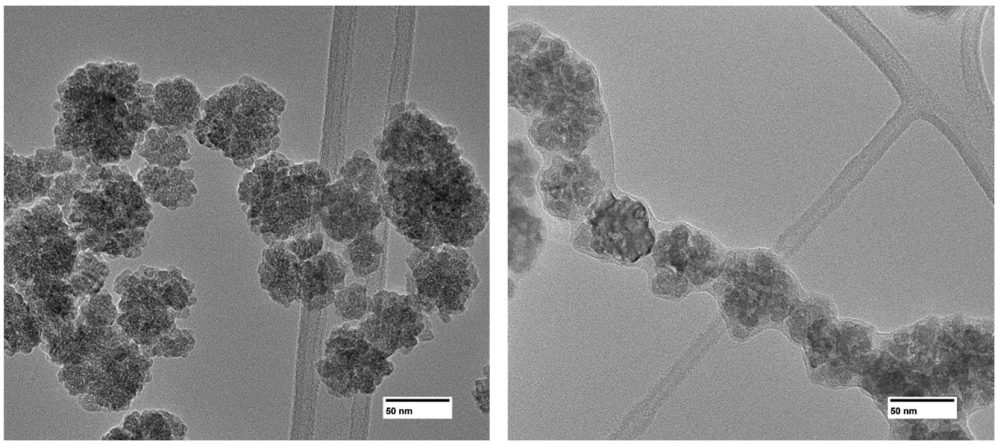

Figure 1. TEM Images of b-Fe_3O_4 (left) and c-Fe_3O_4 (right) NPs.

determined from the kinetic experiments and shaken for the equilibrium times established therein. Upon reaching equilibrium, nanoparticles were removed from the solution using external magnet. The remaining dye concentration was determined by measuring the absorbance of supernatants at the wavelengths of 611 nm and 339 nm for MBlue and CRed, respectively. Concentrations were computed using calibration curves prepared beforehand at identical conditions.

Results and Discussion

Characterization of b-Fe_3O_4 and c-Fe_3O_4 NPs

The size and morphologies of b-$Fe_3O_4$and c-Fe_3O_4 NPs are illustrated in Figure 1 and Figures S1-S2. B-Fe_3O_4 NPs exhibit crystalline structure with an average diameter of approximately 74 ± 16 nm (Figure S1). Following hydrothermal treatment with kraft lignin, an amorphous carbon layer forms around the NPs. Shell thickness was estimated to be 7.2 ± 3.0 nm. The estimate was made based on 63 independent measurements taken from several TEM images in which the boundary between magnetite core and carbon layer was clearly distinguishable. The presence of the carbon coating is also supported by the elemental mapping obtained using Energy-Dispersive X-Ray spectroscopy (EDS). The EDS images reveal that the cores of the c-Fe_3O_4 NPs are primarily composed of iron and oxygen, consistent with magnetite structure, while carbon becomes increasingly predominant toward the particle edges (Figure 2). Collectively, these observations confirm the successful deposition of a carbon shell and demonstrate that the surfaces of b-Fe_3O_4 and c-Fe_3O_4 NPs are both morphologically and elementally distinct.

Multi-point BET specific surface area was estimated to be 71.30 ± 0.21 m^2/g and 12.01 ± 0.06 m^2/g for b-Fe_3O_4 and c-Fe_3O_4 NPs, respectively. We hypothesize that the reduction in surface area is most likely due to the encapsulation of multiple b-Fe_3O_4 NPs within the same shell, as the value is comparable to the reported value of lignin coated nanoparticles of 27.74 m^2/g for a size of 260 nm.[33]

The magnetic properties of both types of NPs were investigated. Figure S3 shows the magnetization curves measured at 300K. The magnetic saturation values are 81.4 and 42.8 emu/g for b-

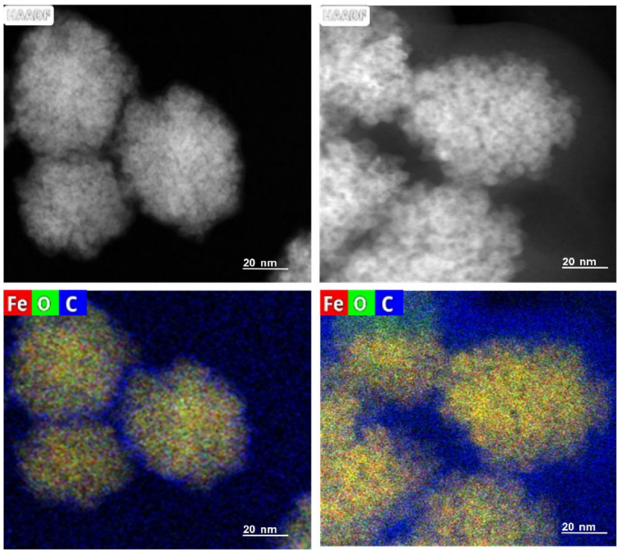

Figure 2. STEM and EDS elemental mapping of b- Fe_3O_4 (left) and c- Fe_3O_4 (right) NPs.

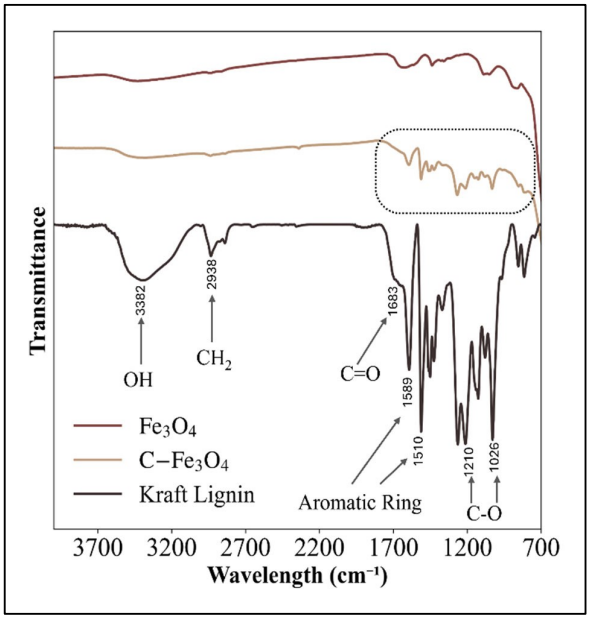

Figure 3. FTIR spectra of Kraft lignin, b-Fe_3O_4 and c-Fe_3O_4 NPs.

View Article Online
DOI: 10.1039/D6NR00230G

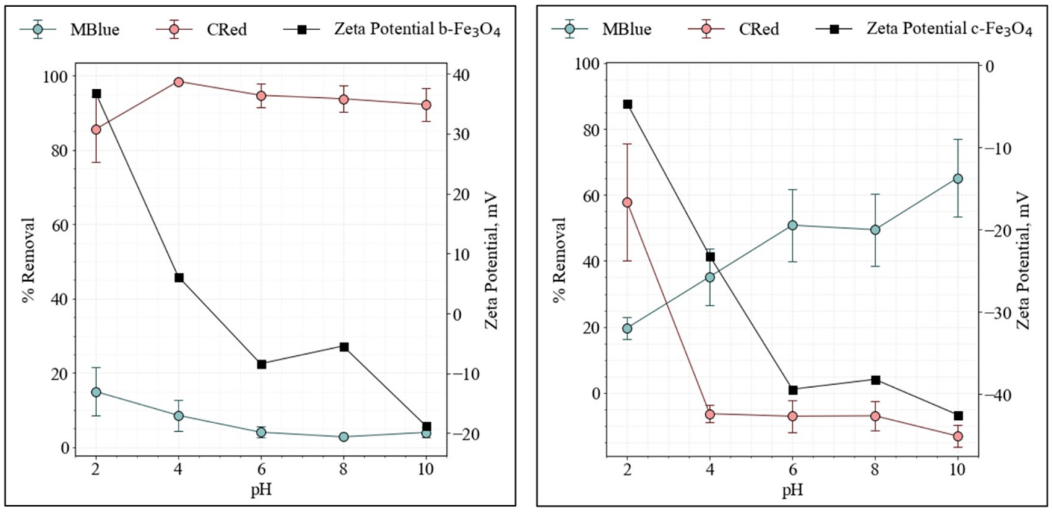

Figure 4. Removal efficiency of cationic and anionic dyes on b-Fe_3O_4 (left) and c-Fe_3O_4 (right) NPs and zeta potential as a function of pH.

Fe_3O_4 and c-Fe_3O_4 NPs, respectively. The reduction in magnetization is attributed to the presence of carbon shell and is consistent with other literature works.[12,28]

To elucidate the surface chemical composition, FTIR spectra were collected for Kraft lignin, b-Fe_3O_4, and c-Fe_3O_4 NPs (Figure 3). For Kraft lignin, a wide absorption band at ~3382 cm^{-1} was attributed to aromatic and aliphatic OH groups. The absorption peaks at 2938 cm^{-1} and 2842 cm^{-1} were assigned to C–H stretching in methyl, methylene and methoxy groups. The absorption peak at ~1683 cm^{-1} was assigned to carbonyl stretching. The absorption peaks at 1589 cm^{-1} and 1510 cm^{-1} were assigned to aromatic ring vibrations. The adsorption peaks at 1210 cm^{-1} and 1026 cm^{-1} were attributed to C-O stretching. The assignment of peaks for Kraft lignin was done in accordance with previously published data.[34] Compared to b-Fe_3O_4, the FTIR spectrum of c-Fe_3O_4 NPs clearly reveals absorption peaks in the 1600 – 1500 cm^{-1} region, which are absent in b-Fe_3O_4 NPs and correspond to C-C stretching vibrations of aromatic rings. These features closely resemble those observed in the FTIR spectrum of Kraft lignin, indicating that some of the lignin-derived functional groups are retained after the shell formation. The persistence of aromatic C-C vibrations supports the successful formation of a lignin-based carbon shell and is particularly significant, as they are expected to facilitate adsorption of aromatic organic contaminants via π–π interactions. The relative intensity of these aromatic bands is reduced compared to pristine kraft lignin, consistent with partial carbonization.

To determine crystal structure, XRD patterns were identified for both types of NPs. The patterned peaks were identified at 18.3°, 30.1°, 35.4°, 43.1°, 53.4°, 56.9°, and 62.5°, which correspond to magnetite Fe_3O_4 (Figure S4). The crystallographic patterns of c-Fe_3O_4 resemble closely those of b-Fe_3O_4, suggesting that the magnetite crystal structure is not affected during the formation of carbon shell.

Adsorption Studies of c-Fe_3O_4 and b-Fe_3O_4 NPs

The effects of pH

The removal efficiency of both types of magnetite NPs was studied as a function of pH in the range 2 to 10. The pH media plays an important role in the removal efficiency of ionic molecules because of the ionization effects at the surface of nanoparticles.

B-Fe_3O_4 NPs exhibited large positive (>30 mV) zeta potential at low pH and negative zeta potential at high pH values (Figure 4). This observation is typically attributed to the protonation and de-protonation of surface Fe-OH groups in response to varying pH. Magnetite NPs dispersed in aqueous media are believed to be heavily passivated with hydroxyl ($-OH$) groups.[35] At low pH, due to the abundance of hydrogen ions in water, the hydroxyl groups on the surface of Fe_3O_4 NPs tend to protonate, resulting in positively charged $-OH_2^+$ on the surface and a positive zeta potential.[7,36] An opposite effect, called de-protonation, takes place when nanoparticles are placed in media with high pH. Hydroxyl groups in water compete with hydroxyl groups on the surface of the Fe_3O_4, with the former pulling hydrogen away and leaving a negatively charged $-O^-$ layer on the surface. Additionally, c-Fe_3O_4 NPs displayed highly negative zeta potential (>-20 mV) within most of the tested pH range, except for pH 2, where the surface charge is slightly positive (Figure 4). These observations are consistent with other published results.[14] Thus, depending on the charge of the surface layer, bare and carbon-coated magnetite nanoparticles are typically expected to adsorb polar molecules via electrostatic interactions.[37-38] Surprisingly, we find that when interacting with dyes, b-Fe_3O_4 NPs displayed an outstanding adsorption even under conditions when the electrostatic repulsion was anticipated to occur.

Congo Red (CRed), a known anionic dye, is negatively charged due to the sulfonate (SO_3^-) groups present in the molecule. As expected, there was practically zero to no adsorption of CRed on c-Fe_3O_4 NPs along the entire pH range, except for pH 2 (Figure 4). This can be attributed to the strong electrostatic repulsion between the overall negative zeta potential on the surface of c-Fe_3O_4 NPs and the dye's sulfonate

View Article Online
DOI: 10.1039/D6NR00230G

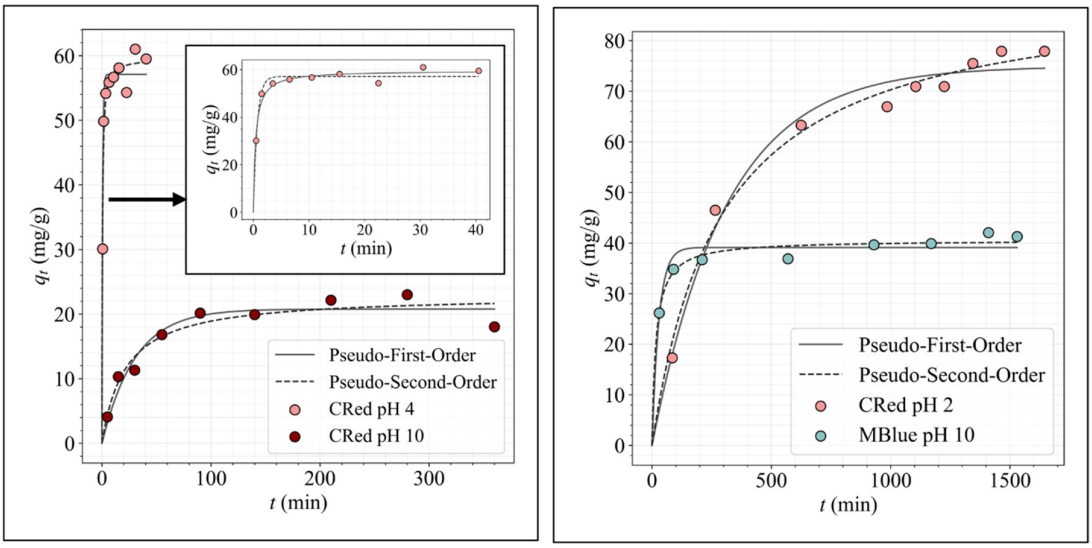

Figure 5. **Left:** Adsorption kinetics of CRed on b-Fe_3O_4 NPs at pH 4 and pH 10. Inset shows a close-up of the pH 4 kinetics. **Right**: Adsorption kinetics of CRed at pH 2 and MBlue pH 10 on c-Fe_3O_4 NPs

groups. The adsorption occurs at pH 2 given that the net surface charge of c-Fe_3O_4 is slightly positive, consistent with the interactions driven by electrostatic forces.

More complex findings were observed in case of b-Fe_3O_4 NPs. The latter demonstrated an exceptionally high adsorption toward anionic CRed dye within the entire 2-10 pH range, regardless of their surface charge (Figure 4). While the adsorption of CRed at low pH can be attributed to strong electrostatic attractions between the positively charged NPs' surface layer and the negatively charged dye's sulfonate groups, this concept fails to explain an exceptionally high removal of CRed at higher pH values, where electrostatic repulsion is anticipated to occur among alike charges. To the best of the authors' knowledge, these findings have not been previously reported. Prior work has reported a decrease in % removal of anionic CRed with increasing pH, which is consistent with electrostatic repulsion of anionic molecules at high pH.[39] In our experiments, the adsorption occurs slower, but the % removal remains high across the entire pH range. The possibility of natural degradation of CRed across the tested pH range has been ruled out experimentally (Figure S5). It is evident that another dominant mechanistic pathway could be responsible for b-Fe_3O_4 NPs to strongly adsorb the anionic dye. These findings are further supported by the interactions with cationic dye.

Methylene blue (MBlue) is a cationic dye with a positively charged dimethylamino group. C-Fe_3O_4 NPs displayed evident adsorption toward MBlue across the pH range of 2 to 10, reaching removal efficiencies of 85% at pH 10. Adsorption of MBlue on c-Fe_3O_4 have been previously attributed to π-π interactions between the aromatic rings on the surface of the c-Fe_3O_4 NPs and the MBlue molecule.[15,31] Note that the estimate for the removal efficiency at pH 2 is approximated, taking into consideration the natural tendency of MBlue to undergo degradation at pH 2 (Figure S6). Additionally, as reflected in the data, c-Fe_3O_4 NPs exhibit higher variability in adsorption capacity, which we attribute to batch-to-batch differences in shell formation. Interestingly, b-Fe_3O_4 NPs exhibited significantly weaker adsorption of cationic MBlue, even under favorable conditions. Specifically, at high pH values, the surface of b-Fe_3O_4 NPs is notoriously negatively charged, meaning that the adsorption of MBlue is expected to occur driven by electrostatic forces among opposite charges. Yet, a very weak adsorption is observed, supporting the presence of an alternative primary mechanism governing the interactions of b-Fe_3O_4 NPs with the ionic dyes.

Adsorption Kinetics

To determine the rate-limiting step and further elaborate the adsorption mechanism, kinetics experiments were performed at the pH values with optimal performances for both types of NPs. The adsorption kinetics were fitted to the most widely used pseudo-first order (PFO) and pseudo-second (PSO) order kinetic models.[40,41] PFO model suggests that the adsorption is predominantly physical in nature and occurs mainly through the diffusion. In contrast, PSO model generally indicates that the adsorption is governed by chemisorption.

PFO: $$\ln(q_e - q_t) = \ln(q_e) - k_1 t$$

PSO: $$\frac{t}{q_t} = \frac{1}{k_2 q_e^2} + \frac{t}{q_e}$$

Here, $q_e\ (mg \cdot g^{-1})$ and $q_t\ (mg \cdot g^{-1})$ are the adsorption capacities of the nanoparticles at equilibrium and at time $t\ (min)$, respectively. The parameters $k_1(min^{-1})$ and $k_2(g \cdot mg^{-1} \cdot min^{-1})$ are the PFO and PSO rate constants. The experimental data was fitted using non-linear least-squares regression implemented via the curve fit function in SciPy. Kinetic models were compared using the combination of correlation coefficients (R^2), Akaike Information Criterion (AIC), and Bayesian Information Criterion (BIC), calculated from the non-linear least-squares residuals.[42] The models'

View Article Online
DOI: 10.1039/D6NR00230G

parameters along with corresponding R^2, AIC, and BIC are summarized in Table 1.

Given that b-Fe_3O_4 NPs demonstrated high removal efficiency with CRed at highly acidic and highly alkaline conditions, the kinetics was studied at both conditextendedions - pH 4 and pH 10 (Figure 5). Note that pH 4 was selected over pH 2 given almost instantaneous adsorption at pH 2, which prevented reliable data collection. Our findings demonstrate that the adsorption of anionic CRed on b-Fe_3O_4 NPs at both pH 4 and pH 10 could be well-fitted by both models, however the differences in AIC and BIC indicate that the models are indistinguishable (ΔAIC/BIC < 2).[43,44] Notably, pH and consequently zeta potential had a
significant effect on the adsorption rates. The adsorption of CRed slowed down considerably with increasing pH. At pH 4, equilibrium was reached within approximately 10 min, whereas adsorption at pH 10 required more than 5 h to attain equilibrium (Figure 5). Furthermore, the equilibrium adsorption capacity (q_e) is also lower for highly alkaline conditions (Table 1). The pronounced differences in rates suggest that the origin of the adsorption process is either unique for each pH or it is the same and is hindered with increasing pH.

In case of c-Fe_3O_4 NPs, the adsorption of both anionic CRed (pH 2) and cationic MBlue (pH 10) is decisively fitted best by the PSO model (Table 1). The application of the shell clearly slowed down the adsorption process even further, requiring more than 24 hours to reach equilibrium in both cases (Figure 5). Note, that the number of NPs was more than doubled for the experiments with coated nanoparticles to combat their slow kinetics. This extended equilibration time may represent a limitation for the practical application of c-Fe_3O_4 NPs in real-world water treatment processes, whereas b-Fe_3O_4 NPs, with their comparatively faster kinetics, may offer a more feasible alternative.

Additionally, the experimental adsorption capacities are generally in good agreement with the adsorption capacities predicted by the kinetic models (Table 1). The only notable exception is the case of CRed adsorption on c-Fe_3O_4 NPs at pH 2, where experimental qe aligns more closely with the value predicted by the PFO, whereas the PSO model was identified as the best-fitting model. This discrepancy may indicate that either the true equilibrium was not reached during the experiment or that the difference in goodness-of-fit between the PFO and PSO models is marginal, making it difficult to unambiguously identify the most appropriate kinetic model.

Equilibrium Isotherm Studies

Equilibrium isotherms were obtained under the same conditions as the kinetic experiments. The experimental data was fitted using the Langmuir and Freundlich isotherm models to describe the adsorption behaviour.[45,46] The Langmuir isotherm,

$$q_e = \frac{q_{max} K_L C_e}{1 + K_L C_e}$$

assumes monolayer adsorption on a homogeneous surface with a finite number of identical adsorption sites, whereas the Freundlich isotherm,

$$q_e = K_F C_e^{1/n},$$

describes adsorption on heterogeneous surfaces and allows for multilayer formation. q_{max} $(mg \cdot g^{-1})$ and q_e $(mg \cdot g^{-1})$ are the maximum and equilibrium adsorption capacities. K_L, K_F and $1/n$ are the constants for the respective models.

At pH 4, the rapid uptake of anionic CRed by b-Fe_3O_4 NPs is best described by the Langmuir model, indicating monolayer surface coverage (Figure 6**,** Table S1). This behaviour suggests that the adsorption proceeds until the available surface sites are saturated, after which equilibrium is reached. In contrast, the adsorption data of the same process at pH 10 follows the Freundlich model, consistent with the multilayer adsorption. This observation implies that once CRed molecules initially anchor to the b-Fe_3O_4 surface, further adsorption proceeds via intermolecular interactions and dye self-assembly process. Interestingly, the adsorption of either cationic MBlue (ph 10) or anionic CRed (pH 2) is also best fitted by Freundlich model. We hypothesize that the adsorption process here begins with the π-π interactions between aromatic regions of the carbon shell and

Table 1. Adsorption kinetic parameters and conditions of b-Fe_3O_4 and c- Fe_3O_4

Adsorbent	Dye	pH	Dosage (mg)	PFO				PSO				Experiment
				R^2	q_e	AIC	BIC	R^2	q_e	AIC	BIC	q_e
b-Fe_3O_4	CRed	4	20	0.957	57.68	17.25	17.65	0.973	62.33	17.49	17.88	54.24
	CRed	10	20	0.955	21.68	12.85	13.24	0.977	24.85	13.36	13.24	20.65
c-Fe_3O_4	CRed	2	50	0.976	74.90	23.10	23.50	0.986	90.60	18.46	18.85	77.88
	MBlue	10	50	0.822	39.11	15.15	15.31	0.930	40.57	7.70	7.86	40.88

View Article Online
DOI: 10.1039/D6NR00230G

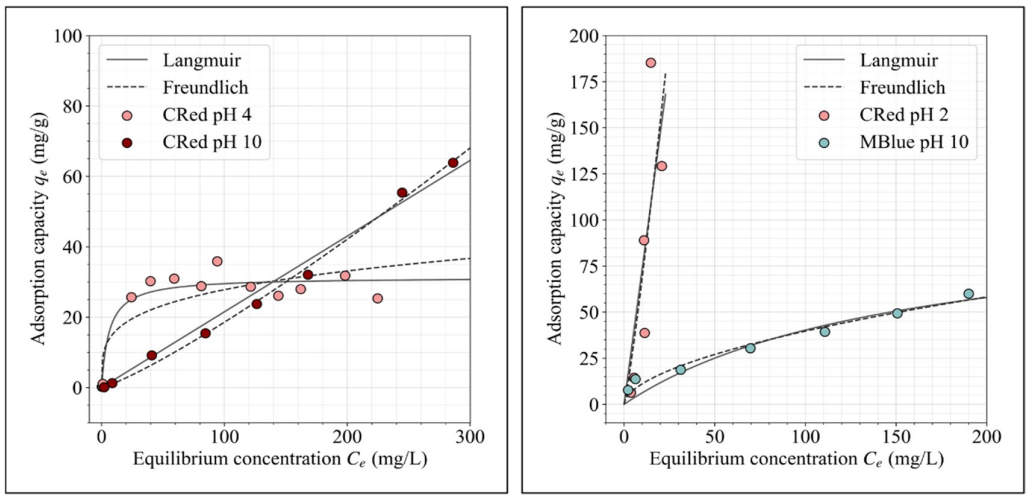

Figure 6. **Left**: Equilibrium isotherms with Langmuir and Freundlich adsorption isotherm models for CRed adsorption on b-Fe_3O_4 NPs at pH 4 and pH 10. **Right:** Equilibrium isotherm with Langmuir and Freundlich adsorption isotherm models for CRed adsorption on c-Fe_3O_4 NPs at pH 2 and pH 10.

dye molecules and is then facilitated by the self-assembly of the dye molecules.

Adsorption Mechanism

Iron oxide magnetite has a complex inverse spinel structure where Fe^{3+} ions occupy tetrahedral sites, while both Fe^{2+} and Fe^{3+} ions occupy octahedral sites. The octahedral sites are often exposed to the surface making them crucial for surface reactions. While both divalent and trivalent ions are available at the surface, it has been previously reported that Fe^{2+} tends to oxidize at the surface of magnetite to Fe^{3+}.[47] We postulate that the b-Fe_3O_4 NPs adsorb ionic dyes predominantly via complexation with localized uncoordinated iron Fe^{3+} cites at the magnetite surface (Table 2). Our hypothesis is strongly supported by an exceptionally high adsorption of anionic CRed on b-Fe_3O_4, regardless of the nanoparticles' net surface charge, excluding electrostatic interactions as the primary mechanism. Though the adsorption is dominated by the surface complexation, the electrostatic interactions have a profound effect on the adsorption rate. As an example, at higher pH the access of dye molecules to Fe^{3+} sites is hindered by the electrostatic repulsion due the negatively charged $-O^-$ on the surface, thus resulting in a considerably slower adsorption rate and lower adsorption capacity.

Additionally, low adsorption of MBlue on b-Fe_3O_4 NPs indicates that adsorption is not driven by nonspecific surface interactions but instead depends on the chemical affinity of CRed to surface Fe^{3+} sites. Collectively, these observations support a mechanism in which CRed binds directly to reactive iron sites on the magnetite surface.

The mechanism of complexation with iron sites is further supported by the drastic reduction in CRed uptake upon application of a carbon shell, which effectively masks or passivates the reactive Fe^{3+} sites and results in a slower uptake of CRed, which is governed most likely via π–π interactions. Noteworthy, the adsorption becomes increasingly unfavourable as the solution pH rises and the zeta potential becomes highly negative. Increasing pH enhances electrostatic repulsion as the dye approaches the negatively charged shell surface, thereby inhibiting close contact and quenching π–π stacking interactions. Collectively, these results indicate that shell-coated systems rely on weaker and slower, pH-sensitive interactions for dye adsorption, whereas bare magnetite adsorbs primarily via surface complexation with uncoordinated iron sites. Authors would like to acknowledge that the proposed adsorption mechanisms are hypothetical and cannot be decisively established without additional investigation, including adsorption-desorption studies, post-adsorption spectroscopic analysis (e.g., FTIR, XPS), and thermodynamic evaluation.[48]

Table 2. Summary of the proposed adsorption mechanisms

System	Kinetics and Isotherm	Plausible Dominant Mechanism
b-Fe_3O_4 CRed (pH 4)	Fast, monolayer	Fe^{3+}-surface complexation, enhanced by electrostatic attraction
b-Fe_3O_4 CRed (pH 10)	Slower, multilayer	Fe^{3+}-surface complexation, accompanied by π–π interactions between dye molecules
c-Fe_3O_4 CRed (pH 2)	Very slow, multilayer	π–π interactions between shell and dye molecules
c-Fe_3O_4 MBlue (pH 10)	Very slow, multilayer	π–π interactions between shell and dye molecules

Conclusions

In this work, a comparative analysis of the adsorption of cationic and anionic dyes on b-$Fe_3O_4$and c-Fe_3O_4NPs was performed. Our findings reveal that standalone magnetite NPs significantly outperform carbon-coated structures, in terms of both adsorption kinetics and capacity, with anionic CRed dye. The

View Article Online
DOI: 10.1039/D6NR00230G

adsorption experiments demonstrate that b-Fe_3O_4 NPs display strong affinity toward anionic CRed across a wide pH range (2-10). Notably, high adsorption occurs at pH 10, even though the net surface charge of magnetite is negative, and electrostatic repulsion of the anionic dye is expected to occur. However, at pH 10 the adsorption rate is more than an order of magnitude slower, and the adsorption capacity decreases by approximately a factor of three compared to pH 4. The slower kinetics and reduced capacity at higher pH are attributed to electrostatic repulsion between negatively charged dye molecules and the magnetite surface. In contrast, b-Fe_3O_4 NPs demonstrate poor adsorption capacity toward cationic MBlue across the studied pH range. Taken together, these observations suggest that the primary adsorption mechanism on b-Fe_3O_4 is most likely surface complexation with uncoordinated iron Fe^{3+} sites. The adsorption of cationic MBlue is substantially improved with the introduction of carbon shell. For c-Fe_3O_4 NPs, the adsorption improves with increasing pH and reaches its maximum at pH 10, which is attributed to the increasingly negative surface charge which favors electrostatic attraction of the cationic dye. In contrast, the adsorption of anionic CRed on c-Fe_3O_4 NPs is negligible, except at pH 2. Although the adsorption capacity of c-Fe_3O_4 is slightly higher than that of b-Fe_3O_4, significantly longer times are required to reach equilibrium. While the carbon shell enables adsorption of both cationic and anionic dyes on the c-Fe_3O_4 surface, the process requires more than 24 hours to reach equilibrium. We hypothesize that the application of carbon shell masks the uncoordinated Fe^{3+} sites on the magnetite surface, thereby altering the adsorption mechanism from surface complexation to π-π interactions. This transition leads to much slower pH-sensitive adsorption of ionic molecules.

Author contributions

Kajibanga conducted experiments, analysed results and wrote the manuscript. Ngah and Walden assisted in conducting and analysing experiments. Morrell supervised experiments and wrote the manuscript.

Conflicts of interest

There are no conflicts to declare.

Acknowledgements

This work was partially supported by the North Dakota Department of Agriculture (grant number 25-432) and University of North Dakota seed grant. The authors would like to thank Sergey Shilov (Bruker Scientific, LLC) for the acquisition of the FTIR spectra, Scott Payne (North Dakota State University) for the acquisition of TEM images, Neil Dilley for the acquisition of magnetic properties (Birck Nanotechnology Center at Purdue University), and Rawan Makhlouf (Particle Technology Labs) for BET specific surface area measurements. The authors would also like to acknowledge the University of North Dakota's Nanofoundry for providing access to their research facilities.

References

1 H. Zhao, H.J. Cui and M.L. Fu, *J. Colloid Interface Sci.*, 2016, **461**, 20.
2 S. Xuan, L. Hao, W. Jiang, X. Gong, Y. Hu and Z. Chen, *Nanotechnology*, 2007, **18**, 035602.
3 L. Kong, X. Lu, X. Bian, W. Zhang and C. Wang, *ACS Appl. Mater. Interfaces*, 2011, **3**, 35.
4 Z. Wang, H. Guo, Y. Yu and N. He, *J. Magn. Magn. Mater.*, 2006, **302**, 397.
5 F.A. Petrie, J. M. Gorham, R.T. Busch, S.O. Leontsev, E.E. Ureña-Benavides and E.S. Vasquez, *Int. J. Biol. Macromol.*, 2021, **181**, 313.
6 X.B. Zhang, H.W. Tong, S.M. Liu, G.P. Yong and Y.F. Guan, *J. Mater. Chem. A*, 2013, **1**, 7488.
7 X. Liu, M.D. Kaminski, Y. Guan, H. Chen, H. Liu and A.J. Rosengart, *J. Magn. Magn. Mater.,* 2006, **306**, 248.
8 G. Magnacca, S. Allera, E. Montoneri, L. Celi and E. Prevot, *ACS Sustain. Chem. Eng.*, 2014, **2**, 1518.
9 G. Bayramoglu, A. Akbulut, G. Liman and M. Y. Arica, *Chem. Eng. Res. Des.*, 2017, **124**, 85–97.
10 X.W. Wei, G. Zhu, C.J. Xia, Y. Ye, J. Wu and P. Du, *Nanotechnology*, 2006, **17**, 4307.
11 K. Petcharoen and A. Sirivat, *Mater. Sci. Eng. B*, 2012, **177**, 421.
12 Y. Gong, L. Wang, J. Liu, J. Tang and D. Zhao, *Sci. Total Environ.*, 2016, **562**, 191.
13 X. Zhao, Y. Shi, Y. Cai and S. Mou, *Environ. Sci. Technol.*, 2008, **42**, 1201.
14 X. Zhao, Y. Cai, F. Wu, Y. Pan, H. Liao and B. Xu, *Microchem. J.*, 2011, **98**, 207.
15 X. Li, Y. He, H. Sui and L. He, *Nanomaterials*, 2018, **8**, 162.
16 Y. Liu, J. Li, W. Zhang and X. Lu, *Environ. Sci. Technol.*, 2018, **52**, 7350–7358.
17 Y. Xu, X. Zhao, W. Zhang and J. Li, *J. Hazard. Mater.*, 2020, **384**, 121352.
18 S. Li, L. Liu, Y. Yu, G. Wang, H. Zhang and A. Chen, *J. Alloys Compd.*, 2017, **698**, 20–26.
19 Z. Duan, W. Zhang, M. Lu, Z. Shao, W. Huang, J. Li, Y. Li, J. Mo, Y. Li and C. Chen, *Carbon*, 2020, **167**, 351–363.
20 B. Kakavandi, A.J. Jafari, R.R. Kalantary, S. Nasseri, A. Ameri and A. Esrafily, *Iran. J. Environ. Health Sci. Eng.*, 2013, **10**, 19.
21 A. Jangra, J. Singh, R. Khanna, P. Kumar, S. Dua, R. Kumar. *Asian J. Chem.*, 2021, **33**, 12, 3031-3038
22 J. Fresnais, M. Yan, J. Courtois, T. Bostelmann, A. Bée, J.F. Berret. *J. Colloid Interface Sci.*, 2013, **395**, 24-30.
23 Y. S. Ho, C. T. Huang and H. W. Huang, *Colloids Surf., A*, 2013, **434**, 256–262.
24 H. Li, H. Jin, R. Li, J. Hua, Z. Zhang and R. Li, *Sci. Rep.*, 2024, **14**, 1217.
25 V.S. Munagapati, H.Y. Wen, A.R.K. Gollakota, J.C. Wen, C.M. Shu, K.Y.A. Lin, Z. Tian, J.H. Wen, G.M. Reddy and G.V. Zyryanov, *J. Mol. Liq.*, 2022, **345**, 118255.

View Article Online
DOI: 10.1039/D6NR00230G

26 S. Chatterjee, N. Guha, S. Krishnan, A.K. Singh, P. Mathur and D.K. Rai, *Sci. Rep.*, 2020, **10**, 111.

27 Z. Zhang and J. Kong, *J. Hazard. Mater.* 2011, **193**, 325–329.

28 O.S. Ivanova, I.S. Edelman, C.R. Lin, E.S. Svetlitsky, A.E. Sokolov, K.A. Lukyanenko, A.L. Sukhachev, N.P. Shestakov, Y.Z. Chen and A.A. Spivakov. *Materials*, 2023, **16**, 23.

29 B. Wang, D. Sun, T.Q. Yuan, G. Song and R.C. Sun, A*CS Symp. Ser.*, 2021, **1377**, 143.

30 L. Fang, H. Wu, Y. Shi, Y. Tao and Q. Yong, *Front. Bioeng. Biotechnol*., 2021, **9**, 691528.

31 Y. Li, M. Wu, B. Wang, Y. Wu, M. Ma and X. Zhang, *ACS Sustain. Chem. Eng.*, 2016, **4**, 5523.

32 H. Deng, X. Li, Q. Peng, X. Wang, J. Chen and Y. Li, *Angew. Chem. Int. Ed.*, 2005, **44**, 2782.

33 S. Li, X. Li, S. Li, P. Xu, Z. Liu and S. Yu, *Int. J. Biol. Macromol.*, 2024, **259**, 128971.

34 M.N.M. Ibrahim, N. Zakaria, C.S. Sipaut, O. Sulaiman and R. Hashim, *Carbohydr. Polym.*, 2011, **86**, 112-119.

35 F. Kraushofer, F. Mirabella, J. Xu, J. Pavelec, J. Balajka, M. Müllner, N. Resch, Z. Jakub, J. Hulva, M. Meier, M. Schmid, U. Diebold and G.S. Parkinson, *J. Chem. Phys*., 2019, **151**, 154702.

36 I.J. Bruce, J. Taylor, M. Todd, M.J. Davies, E. Borioni, C. Sangregorio and T. Sen, *J. Magn. Magn. Mater.*, 2004, **284**, 145.

37 B. Gu, J. Schmitt, Z. Li, L. Chen and J. J. McCarthy, *Environ. Sci. Technol.*, 1994, **28**, 38.

38 A.M. Vindedahl, J.H. Strehlau, W.A. Arnold and R.L. Penn, *Environ. Sci.: Nano*, 2016, **3**, 494.

39 N.T. Nguyen, V.A. Nguyen and T.H. Nguyen, *J. Dispers. Sci. Technol*., 2023, **44** (11), 2161–2168.

40 S. Lagergren, K. Sven. Vetensk. Handl., 1898, **24** (4), 1-39.

41 Blanchard, G., Maunaye, M., Martin, G., *Water Res.,* 1984, **18** (12), 1501-1507.

42 J.P. Vareda, *J. Mol. Liq.*, 2023, **376**, 121416.

43 K.P. Burnham and D.R. Anderson, *Model Selection and Multimodel Inference: A Practical Information-Theoretic Approach*, 2nd ed., Springer, 2002.

44 R.E. Kass and A.E. Raftery, *J. Am. Stat. Assoc.*, **1995**, *90*, 773-795.

45 I. Langmuir, *J. Am. Chem. Soc.*, 1918, **40** (9), 1361-1403.

46 H. Freundlich, Z Phys. Chem, 1906, **57**, 385-471.

47 R.L. Rebodos and P.J. Vikesland, *Langmuir*, 2010, **26**, 16745.

48 H.N. Tran, S.J. You, A. Hosseini-Bandegharaei, and H.P. Chao, *Water Res.*, 2017, **120**, 88e116.

View Article Online
DOI: 10.1039/D6NR00230G

TEM images, FTIR spectra, BET surface area, magnetic properties, python codes for all figures are available: https://gitlab.com/MariaMorrell/rsc-nanoscale-reassessing-the-role-of-carbon-shells-in-magnetite-nanoparticles-a-comparative-adsorption-study-of-ionic-dyes